

Photothermally responsive conductive hydrogels for dual-mode self-sensing soft actuators

Chengnan Qian¹, Ping Guo¹, Ruofei Wang, Xuanzi Luo, Yang Yu, Lin Cheng^{*}, Aiping Liu^{*}

Zhejiang Key Laboratory of Quantum State Control and Optical Field Manipulation, Department of Physics, Zhejiang Sci-Tech University, Hangzhou 310018, China



ARTICLE INFO

Keywords:
Conductive hydrogel
Co-solvent effect
Dual-mode self-sensing
Photothermal actuation
Near-infrared response

ABSTRACT

Multifunctional hydrogels have emerged as promising candidates for advanced applications in soft robotics, human-machine interfaces, and intelligent actuators. However, existing systems face critical challenges in simultaneously achieving rapid actuation, mechanical robustness, and multimodal sensing capabilities. Here, we present a co-solvent-engineered poly(N-isopropylacrylamide) hydrogel that addresses these limitations through molecular and structural optimization. The dimethyl sulfoxide/water binary solvent system induces a homogeneous network architecture in the hydrogel, yielding a fourfold enhancement in tensile strength while maintaining exceptional responsiveness. Building upon this mechanical foundation, we develop an integrated hydrogel system combining photothermal actuation with dual-mode sensing functionality. The system demonstrates superior strain-sensing performance by integrating a polyaniline piezoresistive layer and a poly(vinylidene fluoride-ran-trifluoroethylene) piezoelectric layer. It is characterized by an extensive detection range of 1–110% stretching strain, a rapid response time of 235 ms, excellent signal linearity, and the capability to simultaneously detect bending direction and velocity. Near-infrared light (808 nm) serves both as the actuation stimulus and control signal, enabling real-time multimodal feedback during operation. This integrated approach to photothermal actuation and dual-mode self-sensing within a single hydrogel platform represents a significant advancement in smart soft material design, with potential applications in adaptive robotics, biomedical devices, and intelligent human-machine interfaces.

1. Introduction

The capacity to perceive environmental stimuli and execute adaptive responses is a fundamental characteristic of biological systems. From the thigmonastic movement of *Mimosa pudica* leaves to the rapid conformational changes in Venus flytrap foliage for prey capture, and even the sophisticated tentacular control mechanisms of cephalopods, these organisms exemplify integrated sensing-actuation systems that have inspired advancements in bioinspired robotics [1]. Recent progress in functional materials science has led to the development of various stimulus-responsive candidates suitable for intelligent actuators, including shape memory alloys [2], liquid crystal elastomers [3], hydrogels [4], and dielectric elastomers [5]. Among these, stimulus-responsive hydrogels emerge as particularly promising candidates due to their multimodal responsiveness to diverse stimuli such as temperature [6,7], electricity [8,9], magnetic fields [10,11], light [12,13], pH [14,15], and their exceptional biocompatibility. These attributes have

facilitated their applications in flexible actuators [16], artificial muscles [17], and soft robotics [18,19]. Poly(N-isopropylacrylamide) (PNIPAM) hydrogel, a representative thermo-responsive system, demonstrates reversible phase transition at its lower critical solution temperature ($LCST \approx 32^\circ\text{C}$) [20] due to the dynamic equilibrium between hydrophilic amide groups and hydrophobic isopropyl moieties in its molecular structure. However, the inherent mechanical fragility and restricted phase transition dynamics significantly constrain its practical implementation in advanced actuator systems.

The ultimate objective in smart material design is to achieve synergistic integration of sensing and actuation within a single monolithic structure—mirroring the unified sensory-motor systems found in biology. While current soft actuators can execute tasks like gripping or motion control with feedback from external sensors [21], they often rely on modular architectures where sensing and actuation are physically decoupled. Conventional soft sensors relying on capacitive [22], triboelectric [23], or piezoresistive [24] principles typically function as

* Corresponding authors.

E-mail addresses: chenglin@zstu.edu.cn (L. Cheng), liuaiping1979@gmail.com (A. Liu).

¹ Authors contribute equally.

separate layers, limiting spatial resolution and real-time responsiveness. Recent efforts to bridge this gap have focused on incorporating photothermal converters, such as carbon nanotubes [25,26], gold nanoparticles [27], and MXene nanosheets [28–31], into thermoresponsive hydrogels. Conductive polymers like polyaniline (PANI) further offer a multifunctional platform due to their electrical conductivity and photothermal efficiency. Prior examples, including F-PNIPAAm/PANI composites [32] and ice-templated PANI/PNIPAM hybrids [33], have demonstrated some degree of self-sensing behavior. Despite significant progress in hydrogel-based soft actuators with integrated actuation-sensing capabilities [34], most systems are still limited to uniaxial sensing and lack the capacity to detect complex, multidimensional stimuli. Piezoresistive sensors can effectively monitor deformation magnitude and static force distribution in real time, but they are generally incapable of identifying force directionality or capturing dynamic strain-rate responses. These limitations are particularly critical in soft robotic systems that require precise control over spatiotemporal force feedback during interaction with complex environments. Therefore, there is a pressing need for advanced intelligent materials that can simultaneously achieve multiaxial force sensing and programmable mechanical responses, enabling more sophisticated and adaptive soft robotic platforms.

Here, we introduce a multifunctional hydrogel platform that addresses these limitations by integrating photothermal actuation, piezoresistive strain sensing, and piezoelectric dynamic sensing within a single material system. The hydrogel is synthesized using a dimethyl sulfoxide (DMSO)/water co-solvent system that induces a highly porous network via competitive hydrogen bonding, yielding significant improvements in mechanical strength (4-fold increase in tensile strength and 1.9-fold higher Young's modulus compared to pure solvent systems). Through a low-temperature one-pot method, polyaniline (PANI) is incorporated to construct an interpenetrating conductive network, enabling dual-mode sensing and NIR-triggered actuation. Furthermore, the integration of a poly(vinylidene fluoride-trifluoroethylene) (P(VDF-TrFE)) layer provides a piezoelectric component that enables dynamic, directional force detection during bending deformations. This trifunctional system enables closed-loop operation by combining: (1) rapid photothermal actuation, (2) real-time piezoresistive strain sensing, and (3) bidirectional piezoelectric voltage output under dynamic mechanical stimuli. This integrated approach lays the foundation for next-generation soft robotics with enhanced environmental adaptability, closed-loop control, and biomimetic intelligence.

2. Experimental section

2.1. Materials

N-Isopropylacrylamide ($C_6H_{11}NO$, 98%), *N,N*-methylenebis(acrylamide) ($C_7H_{10}N_2O_2$, AR), photoinitiator Darocur 1173 ($C_{10}H_{12}O_2$, AR), hydrochloric acid (HCl, 37%), glutaraldehyde ($C_5H_8O_2$, AR) were purchased from Shanghai Aladdin Biochemical Technology Co., Ltd. (China). Poly(vinyl alcohol) 1799 ($[C_2H_4O]_n$, hydrolysis >99%), Dimethyl sulfoxide (C_2H_6OS , AR), aniline (C_6H_7N , AR), ammonium persulfate ($(NH_4)_2S_2O_8$, AR) and *N,N*-dimethylformamide (C_3H_7NO , AR) were supplied by Shanghai McLean Biochemical Co., Ltd. (China). Polyvinylidene fluoride (vinylidene fluoride) ($(C_2H_2F_2)_n(C_2HF_3)_m$, 7:3) was obtained from the French chemical company Arkema.

2.2. Preparation of $(PVA)_xPNIPAM_y$ hydrogels

Initially, 10 g of PVA was dissolved in 90 mL of deionized water by heating in a 95 °C water bath with continuous stirring for 5 h until complete dissolution, yielding a clear and transparent 10% PVA solution. Subsequently, 20 mg crosslinking agent BIS, 1 g NIPAM, and 25 µL Darocur 1173 were dissolved in a mixed solvent containing 3 mL DMSO and 1 mL deionized water. After obtaining a homogeneous solution, 1

mL of the 10% PVA solution was incorporated under continuous stirring to form a transparent hydrogel precursor solution. The prepared precursor solution was subsequently injected into a custom mold consisting of two glass slides (60 mm × 25 mm) separated by a silicone spacer (40 mm × 10 mm × 1.5 mm). Following injection, the mold was irradiated 15 cm below a 250 W UV lamp ($\lambda = 365$ nm) in an ice-water bath for 5 min to complete photopolymerization. After curing, the $(PVA)_xPNIPAM_y$ composite hydrogel was carefully demolded, thoroughly rinsed with deionized water to remove surface residues, and stored in a humid environment for subsequent use. The hydrogels were designated as $(PVA)_xPNIPAM_y$, where x and y represented the mass ratios of PVA in the reaction system and the proportion of DMSO in the solvent system, respectively. For instance, $(PVA)_2PNIPAM_{0.6}$ indicated a PVA concentration of 2% with 60% DMSO in the solvent system.

2.3. Preparation of $(PVA)_xPNIPAM_y/PANI_z$ hydrogels

First, 4.564 g ammonium persulfate (APS) was dissolved in deionized water under continuous stirring and subsequently diluted to a final volume of 10 mL to achieve a 2 mol/L APS solution. This solution was then precooled at 4 °C in a refrigerator for later use. Next, 1 g NIPAM, 20 mg BIS, and 25 µL Darocur 1173 were thoroughly dissolved in 3 mL DMSO through vigorous stirring. To this mixture, 138 µL aniline, 0.42 mL HCl (37%), and 1 mL 10% PVA solution were sequentially added while maintaining the reaction mixture in an ice-water bath. Finally, 0.5 mL of the precooled APS solution was introduced, followed by rapid stirring for 1 min to ensure homogeneity. The resulting precursor solution was injected into a custom mold consisting of two glass slides (60 mm × 25 mm) separated by a silicone spacer (40 mm × 10 mm × 1.5 mm). The assembled mold was irradiated 15 cm below a 250 W UV lamp ($\lambda = 365$ nm) in an ice-water bath for 5 min to initiate photopolymerization. After light curing, the mold was transferred to a 4 °C refrigerator for 72 h to facilitate low-temperature polymerization of aniline. Following demolding, the $(PVA)_xPNIPAM_y/PANI_z$ composite hydrogel was extensively rinsed with deionized water to remove unreacted residues, then stored in a humid environment for subsequent characterization. The hydrogels were labeled as $(PVA)_xPNIPAM_y/PANI_z$, where x, y, and z denoted the mass ratios of PVA, proportion of DMSO in mixed solvent solvent, and the content of crosslinking agent BIS, respectively. For example, $(PVA)_2PNIPAM_{0.6}/PANI_{0.2}$ indicated a system containing 2% PVA, 60% DMSO in the solvent, and 20 mg BIS as crosslinker.

2.4. Preparation of P(VDF-TrFE) piezoelectric films

The P(VDF-TrFE) films were fabricated via a solution casting method. Initially, P(VDF-TrFE) powder was dissolved in *N,N*-dimethylformamide (DMF) at a 1:20 (w/w) ratio. The mixture was heated in a 60 °C water bath with continuous stirring for 3 h to obtain a homogeneous colorless solution. The solution was then drop-cast onto a glass mold consisting of a glass plate and a silicone spacer (10 cm × 10 cm × 0.1 cm). A spatula was used to uniformly spread the solution, after which the mold was transferred to an 80 °C oven for 30 min to evaporate residual solvent. Subsequently, the film was annealed at 120 °C for 2 h to enhance crystallinity, cooled to room temperature, and carefully demolded. To induce piezoelectric properties, the annealed film was immersed in silicone oil and polarized under an electric field of 1 kV/mm for 2 h. Finally, the film was thoroughly washed with organic solvents to remove silicone oil residues, yielding the final piezoelectric P(VDF-TrFE) film.

2.5. Preparation of $(PVA)_2PNIPAM_{0.6}/PANI_{0.2}/P(VDF-TrFE)$ bilayer actuator

Initially, the $(PVA)_2PNIPAM_{0.6}/PANI_{0.2}$ hydrogel substrate was affixed to a glass slide. Place the carbon cloth electrode on the hydrogel

to make it closely adhere to the hydrogel. Double-sided tape was placed between the glass slide and the silicone pad to ensure that the silicone pad was elevated 200 μm above the hydrogel surface. A 10% PVA solution was then poured into the mold and cryogenically cured at -20°C for 30 min. Subsequently, a P(VDF-TrFE) piezoelectric thin film layer of the lead-out electrode was laminated onto the PVA layer, followed by a second casting of the 10% PVA solution and an additional cryogenic curing cycle. After the curing process, the construct was removed and allowed to melt at room temperature for 30 min. This freezing-thawing cycle was repeated three times to enhance mechanical stability. The bilayer construct was chemically crosslinked by immersion in a 1 wt% glutaraldehyde solution for 10 h, followed by extensive rinsing with deionized water to eliminate unreacted agents. Finally, the $(\text{PVA})_2\text{PNIPAM}_{0.6}/\text{PANI}_{0.2}/\text{P}(\text{VDF-TrFE})$ actuator was stored in a hydrated state prior to characterization. The electrical connection of the hydrogel is shown in Fig.S1. The carbon cloth electrode is *in situ* fixed in the hydrogel through the PVA layer. The electrodes of the piezoelectric sensor are coated with gold electrodes by magnetron sputtering and then led out through copper wires. When conducting the conductivity test, connect both ends of the carbon cloth to the instrument. When conducting the strain sensing test, connect the carbon cloth and the copper wire to the testing instrument respectively.

2.6. Characterizations

The hydrogel samples were frozen in liquid nitrogen for 20 min and then freeze-dried in a freeze dryer (FD-1C-50, Beijing Boyikang) at -80°C for about 24 h. The morphologies of freeze-dried hydrogels were observed by SEM (S-4800, Hitachi, Tokyo, Japan) under 3 kV accelerating voltage. FTIR data were recorded in the wave number range of 500 to 4000 cm^{-1} on the infrared spectrometer (Thermo Fisher Scientific, Nicolet iS20 series).

2.7. Mechanical property characterization

The mechanical properties of hydrogels were evaluated using a universal testing machine (HY-0230, Shanghai Yiheng Precision Instruments). Samples were clamped via custom fixtures and stretched at a constant rate of 50 mm/min until fracture. Stress-strain curves were automatically recorded by the instrument's software for subsequent analysis.

2.8. Response dynamics test

To quantify the thermoresponsive behaviors of $(\text{PVA})_x\text{PNIPAM}_y$ and $(\text{PVA})_x\text{PNIPAM}_y/\text{PANI}_z$ hydrogel, rectangular specimens ($20\text{ mm} \times 10\text{ mm} \times 1.5\text{ mm}$) were immersed in 60°C deionized water under controlled conditions. The volumetric transition process was monitored using a high-resolution digital camera until dimensional stabilization. Then, the images were intercepted at different time periods and the areas were counted by image software to obtain the area shrinkage rate over time. For statistical rigor, five measurements were taken for each formulation, and the data were expressed as an average.

2.9. Characterization of force-induced deformation sensing

The piezoresistive properties of $(\text{PVA})_x\text{PNIPAM}_y/\text{PANI}_z$ hydrogels were evaluated using a synchronized mechanical-electrical testing system. A universal testing machine (HY-0230, Shanghai Yiheng) equipped with custom grips was programmed to apply different uniaxial pulls while a Keithley 2400 Digital Source Meter (Electrical instrument of China Inspection Department) continuously monitored electrical resistance. The bending of piezoelectric and piezoresistive properties were achieved by fixing the integrated $(\text{PVA})_x\text{PNIPAM}_y/\text{PANI}_z/\text{P}(\text{VDF-TrFE})$ actuator to the cardboard, applying different bending by mechanical tester. The charge amplifier was used to continuously measure the

output voltage and the Keithley 2400 Digital Source was used to measure the resistance change.

2.10. Photothermal response characterization

To characterize the photothermal properties, the $(\text{PVA})_x\text{PNIPAM}_y$ and $(\text{PVA})_x\text{PNIPAM}_y/\text{PANI}_z$ hydrogels ($15\text{ mm} \times 15\text{ mm} \times 2\text{ mm}$) were irradiated with near infrared light (808 nm), with thermal profiles recorded using an infrared thermal imager. For light-driven deformation analysis, one end of the hydrogel strip was clamped in cold water (4°C), while the free end was exposed to NIR light (808 nm, 1 W). The bending process was captured by a digital camera and bending angles at specific timepoints were quantified using ImageJ software. Light irradiation cycles (ON/OFF) were repeated to observe reversible actuation.

2.11. Measurement of light-driven deformation sensing

The $(\text{PVA})_x\text{PNIPAM}_y/\text{PANI}_z$ hydrogels were connected to a Keithley 2400 Digital Source Meter via carbon cloth electrodes and submerged in water with one end fixed. Under NIR irradiation (808 nm), real-time resistance changes during bending were recorded synchronously with optical monitoring. Digital image analysis (ImageJ) was employed to correlate resistance variations with bending angles (0° - 90°) at defined intervals.

3. Results and discussion

3.1. Structural design and co-solvent effect mechanism of smart hydrogel system

The structural design of smart hydrogel systems is critical for achieving controllable functionality and enhanced performance. In conventional synthesis methods, the diffusion of polyaniline (PANI) within the hydrogel matrix is often restricted [35], leading to an inhomogeneous distribution (Fig. 1a and Fig.S2). To overcome this issue, our approach introduced directly ANI, ammonium persulfate (APS), and hydrochloric acid (HCl) into the precursor solution [36]. By employing a low-temperature initiation strategy combined with UV-assisted polymerization, we effectively restrained PANI formation in PNIPAM hydrogel cross-linking network (Fig.S3). This process allows ANI monomers to disperse uniformly and polymerize along the PNIPAM hydrogel scaffold (Fig. 1b), forming uniform and dense conductive network in PNIPAM hydrogel. The conductive mechanism of polyaniline is mainly electronic conduction. Optical images (Fig.S4) confirm the enhanced spatial homogeneity achieved through this low-temperature polymerization method. As shown in Fig. 1c, the molecular structures of PNIPAM, PVA, and PANI, along with their proposed intermolecular interactions, are illustrated. Hydrogen bonding is primarily formed between the hydroxyl (-OH) groups of PVA and the amide (C=O) groups of PNIPAM, as well as between the hydroxyl groups of PVA and the amine (-NH-) groups of PANI. These hydrogen bonds act as physical cross-links that interconnect PVA and PANI within the PNIPAM matrix, thereby enhancing the mechanical integrity and stability of the hydrogel network. DMSO, a more effective solvent for PNIPAM than water, plays a crucial role in modulating the polymer's structural characteristics. During polymerization, DMSO competes with water molecules for adsorption sites [37], displacing water from the polymer chains. Increasing DMSO concentration induces significant conformational changes in the PNIPAM molecular chains, as illustrated in Fig. 1d. As the proportion of DMSO in the solvent increases, enhanced surface hydrophobicity causes PNIPAM chains to collapse into a tightly packed spherical conformation, which is subsequently fixed by chemical cross-linking. As DMSO increasingly dominates the solvent system, competitive solvation diminishes, enabling the polymer chains to revert to a extended coil conformation [38]. This coil-sphere-coil transition, governed by the DMSO-water co-solvent effect, is closely correlated with the

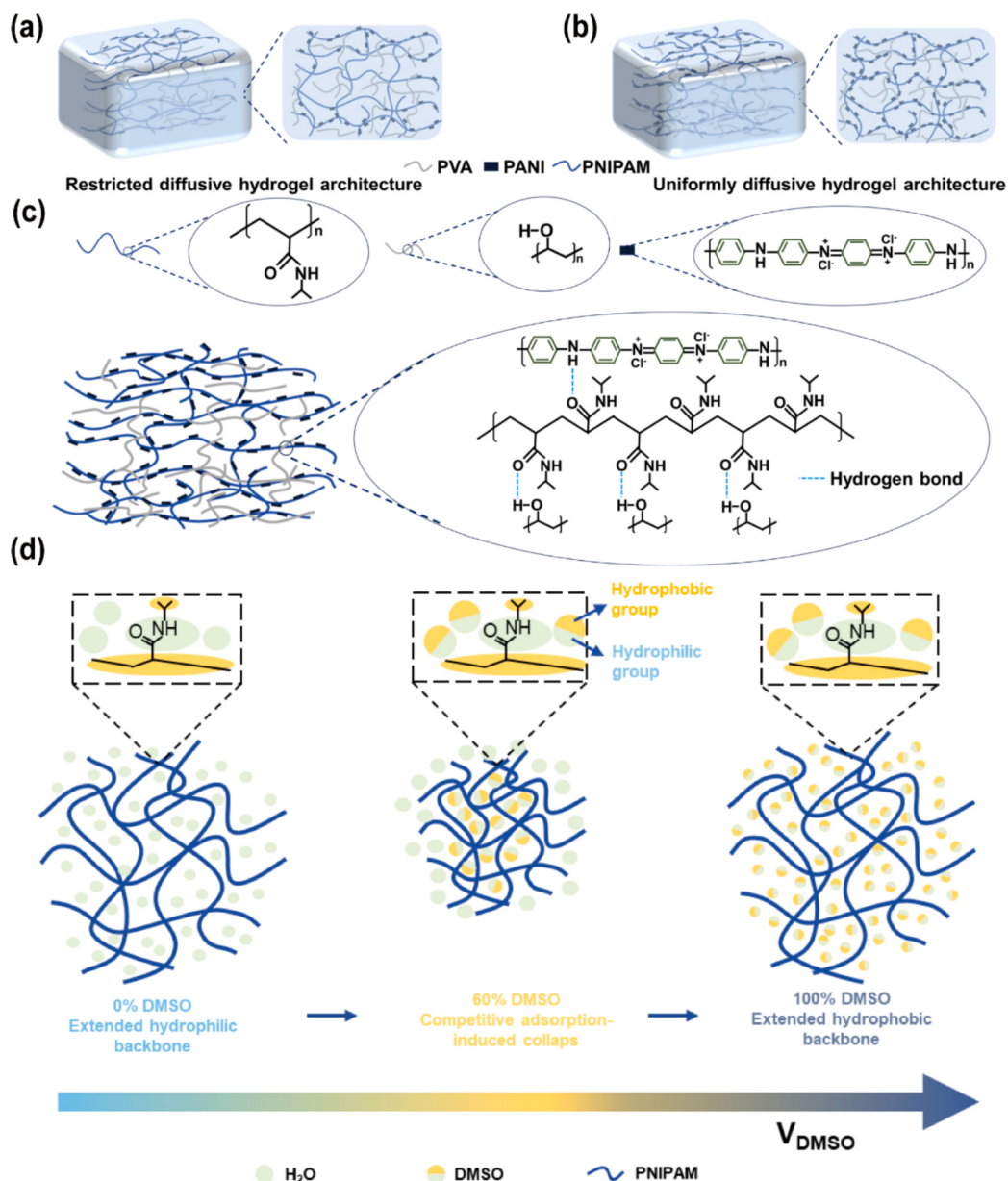


Fig. 1. (a) Illustration of PANI distribution using traditional preparation method. (b) Illustration of PANI distribution by the current synthesis method. (c) The molecular structural formulas of PNIPAM, PVA and PANI and the schematic diagrams of the interactions among their components. (d) Structural transformations of PNIPAM molecular chains as DMSO concentrations increase.

macroscopic optical shift (transparent → white → transparent) observed in Fig.S5. This structural transformation directly influences the hydrogel's mechanical properties and responsiveness, thereby enhancing its sensitivity to external stimuli. By integrating structural optimization with co-solvent engineering, this approach establishes a robust framework for developing smart hydrogel systems with precise actuation, sensing, and adaptive response capabilities.

3.2. Microstructure and mechanical properties of hydrogels

A series of hydrogels were synthesized by systematically varying the proportion of different components. The SEM characterization of freeze-dried samples reveals distinct microstructural differences between hydrogels prepared with pure water solvents and DMSO/water solvents (Fig. 2a-b). The pores polymerized in pure water solvents, resulting in isolated structures (Fig. 2a), are termed closed pores, while the highly interconnected pores formed due to the collapse caused by crosslinking

co-dissolution (Fig. 2b) are referred to as open pores [38]. Specifically, the pure solvent system exhibits a uniform closed-pore structure, whereas the DMSO/water co-solvent induces chain collapse during photopolymerization, resulting in an open-pore architecture. The SEM images of hydrogels prepared with different DMSO concentrations are shown in Fig.S6. To further investigate the effect of solvent composition on hydrogel microstructure, atomic force microscopy (AFM) was performed on hydrogels synthesized in both DMSO/water mixed solvent and pure water (Fig.S7). The AFM images reveal that the hydrogel synthesized in DMSO/water exhibits significant surface height variations, indicative of a more heterogeneous and porous morphology. This is attributed to the competitive hydrogen bonding between DMSO and water, which induces partial polymer chain collapse and phase separation during gelation, resulting in a looser and more disconnected pore network. In contrast, the hydrogel prepared in pure water shows a smoother and more uniform surface, reflecting a denser and more homogeneous polymer network. The most widely accepted explanation for

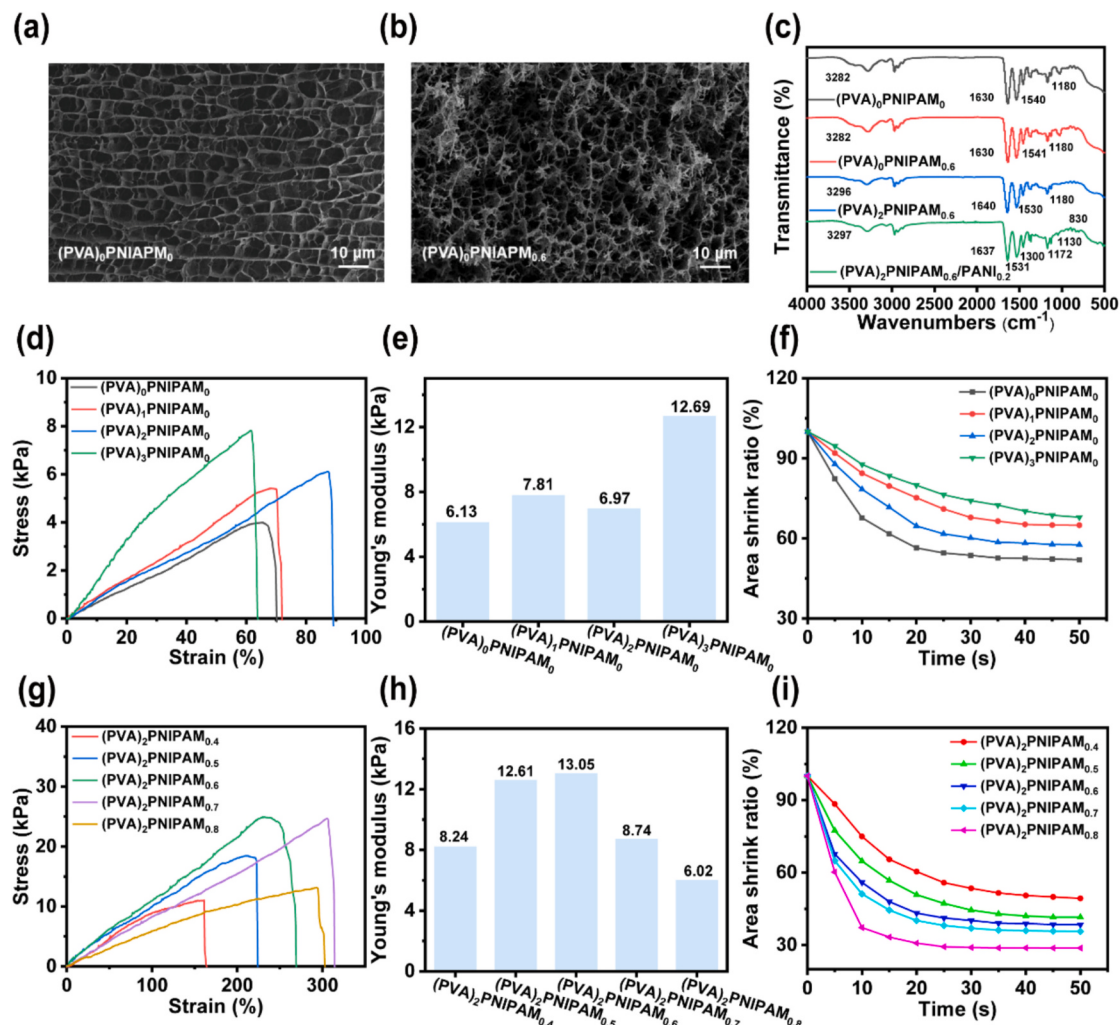


Fig. 2. SEM images of (a) $(\text{PVA})_0\text{PNIPAM}_0$ and (b) $(\text{PVA})_0\text{PNIPAM}_{0.6}$. (c) FTIR spectra of $(\text{PVA})_0\text{PNIPAM}_0$, $(\text{PVA})_0\text{PNIPAM}_{0.6}$, $(\text{PVA})_2\text{PNIPAM}_{0.6}$ and $(\text{PVA})_2\text{PNIPAM}_{0.6}/\text{PANI}_{0.2}$ hydrogels (d) Stress-strain curves, (e) Young's modulus and (f) response kinetics of hydrogels with varying PVA contents. (g) Stress-strain curves, (h) Young's modulus and (i) response kinetics of hydrogels with varying DMSO concentrations.

this structural change is that it results from general competitive adsorption [37]. Notably, since PVA serves only as a strength-enhancing component with a low content, it has no significant impact on the hydrogel structure (Fig.S8). Furthermore, the incorporation of ANI monomer does not alter the open-pore morphology because ANI does not participate in the photopolymerization process of the hydrogels. With increasing BIS content, the composite hydrogels exhibit a more compact microstructure and a more uniform pore size due to their higher crosslinking density (Fig.S9). Fourier Transform Infrared Spectrometer (FTIR) analysis (Fig. 2c) confirms molecular interactions between PNIPAM and poly (vinyl alcohol) (PVA). The characteristic C=O (amide I) and N—H (amide II) vibrations of PNIPAM appear at 1630 cm^{-1} and 1540 cm^{-1} , respectively. The $(\text{PVA})_0\text{PNIPAM}_{0.6}$ hydrogel prepared by the cosolvent effect shows a characteristic peak similar to that of pure $(\text{PVA})_0\text{PNIPAM}_0$, indicating that the DMSO-water mixed solvent primarily modifies the pore structure without significantly altering its chemical composition of the PNIPAM hydrogel. Upon incorporating PVA, these peaks shifted to 1640 cm^{-1} ($+10 \text{ cm}^{-1}$) and 1530 cm^{-1} (-11 cm^{-1}), indicating the formation of hydrogen bonds between the hydroxyl groups of PVA and the carbonyl groups of PNIPAM [39]. Additionally, the characteristic peak at 3282 cm^{-1} shifted to 3296 cm^{-1} after PVA addition. This shift is attributed to stronger hydrogen bonding between the -OH groups in PVA and the C=O groups in PNIPAM, thereby reducing the interaction between the -NH₂ groups

and the C=O groups in PNIPAM [40]. After polyaniline polymerization, a series of characteristic bands are observed at 1300 , 1130 , and 830 cm^{-1} , corresponding to the tensile vibrations of the polyaniline benzene ring [41]. The displacement of the vibration peak at 1180 cm^{-1} was 1172 cm^{-1} (-7 cm^{-1}), and that at 1640 cm^{-1} was 1637 cm^{-1} (-3 cm^{-1}), proving that a hydrogen bond connection was formed between PANI and PNIPAM. The FTIR results indicated that PVA and PANI were introduced into the hydrogel and formed hydrogen bond connections with it. To experimentally validate these interactions, X-ray photoelectron spectroscopy (XPS) was conducted on $(\text{PVA})_0\text{PNIPAM}_{0.6}$, $(\text{PVA})_2\text{PNIPAM}_{0.6}$, and $(\text{PVA})_2\text{PNIPAM}_{0.6}/\text{PANI}_{0.2}$ hydrogels (Fig.S10). In the $(\text{PVA})_0\text{PNIPAM}_{0.6}$ sample, the C 1 s spectrum exhibited a C=O peak at 287.78 eV . Upon the addition of PVA ($(\text{PVA})_2\text{PNIPAM}_{0.6}$), a new C—O peak appeared at 288.88 eV , corresponding to the PVA component, while the C=O peak shifted to 287.68 eV , suggesting hydrogen bonding between PVA and PNIPAM. With the further introduction of PANI ($(\text{PVA})_2\text{PNIPAM}_{0.6}/\text{PANI}_{0.2}$), a C⁺ peak characteristic of PANI was observed at 287.9 eV , and the C=O peak further shifted to 287.48 eV . These progressive spectral shifts confirm the formation of hydrogen bonds between the hydrogel components, supporting the proposed cross-linking mechanism. As shown in Fig. 2d and e, hydrogels without PVA show shorter elongation and lower tensile strength. The addition of PVA enhance both elongation and tensile strength, as well as the Young's modulus of hydrogels. This trend suggests that PVA serves as an

effective reinforcing component, significantly improving the mechanical properties of the hydrogels. In comparing hydrogels with varying PVA content, $(\text{PVA})_2\text{PNIPAM}_0$ demonstrates increased elongation and tensile strength while exhibiting a decreased Young's modulus compared to $(\text{PVA})_1\text{PNIPAM}_0$. These results indicate that as PVA content increases, PVA molecular chains gradually form, enhancing the toughness of the hydrogels and enabling them to withstand greater mechanical loads and deformation. The relatively low Young's modulus also facilitates easier actuation of the hydrogels. However, further increases in PVA content lead to a significant reduction in elongation for $(\text{PVA})_3\text{PNIPAM}_0$ hydrogel, accompanied by a substantial increase in tensile strength and Young's modulus, likely due to PVA crystallization-induced reinforcement [42]. This increased rigidity enhances the maximum stress capacity but substantially reduces strain, thereby limiting the flexibility of the hydrogels. Mechanical and structural characterizations collectively reveal that DMSO concentration critically influences hydrogel performance. FTIR analysis (Fig.S11) shows that in pure water, the C=O stretching vibration of PNIPAM appears at 1660 cm^{-1} due to hydrogen bonding with water. At 60% DMSO, this peak redshifts to 1652 cm^{-1} , indicating stronger interaction between DMSO and PNIPAM via competitive hydrogen bonding. When the DMSO concentration increases to 80%, the peak shifts back to 1654 cm^{-1} , suggesting weakened hydrogen bonding due to DMSO excess. These findings align with SEM results (Fig. 2a and Fig.S6), confirming that 60% DMSO yields the most open and interconnected pore network via DMSO-induced phase separation. Correspondingly, mechanical testing (Fig. 2g-h) shows that hydrogels prepared at this concentration exhibit optimal performance, including a fourfold increase in tensile strength and 1.9-fold increase in Young's modulus compared to aqueous systems. However, beyond 60% DMSO, the reduced phase separation leads to denser networks and mechanical degradation—for example, the Young's modulus of $(\text{PVA})_2\text{PNIPAM}_{0.8}$ drops to 46% of that of $(\text{PVA})_2\text{PNIPAM}_{0.6}$. Thermoresponsive actuation results (Fig. 2f and i) further demonstrate that both pore architecture and modulus govern shrinkage dynamics. While $(\text{PVA})_2\text{PNIPAM}_{0.6}$ achieves a 61% area reduction in 35 s (a 45% faster response than the aqueous counterpart), $(\text{PVA})_2\text{PNIPAM}_{0.8}$, despite diminished porosity, maintains rapid actuation (71% in 35 s) due to its low modulus (6.02 kPa), confirming that lower stiffness promotes faster water transport. This inverse relationship between modulus and actuation efficiency underscores the importance of balancing structural and mechanical design in hydrogel actuators. The $(\text{PVA})_2\text{PNIPAM}_{0.6}/\text{PANI}_{0.2}$ hydrogel demonstrates the highest tensile strain and fastest thermal response among all samples. Its dissipated energy reaches 1920 J/m^3 (Fig.S12), attributed to the synergistic energy dissipation mechanisms: dynamic hydrogen bond breaking/reforming and the sliding or fracture of the PANI conductive network. PANI serves as the primary conductive component, contributing electronic conductivity under solid-state conditions, while ionic conduction is negligible. This electron-dominated transport mechanism defines the hydrogel's overall conductivity. To further understand its thermoresponsive behavior, we quantified the activation energy of the deswelling process using the Arrhenius equation over $40\text{--}70^\circ\text{C}$. The shrinkage kinetics followed a quasi-first-order model, and the Arrhenius analysis yielded an activation energy of 9.24 kJ/mol (Fig.S13). This low activation energy suggests minimal resistance to coordinated molecular chain movement, enabling rapid thermal response. Consequently, the $(\text{PVA})_2\text{PNIPAM}_{0.6}/\text{PANI}_{0.2}$ hydrogel was selected for subsequent experiments. Moreover, the enhanced mechanical strength results from the in situ polymerization of PANI within the PNIPAM matrix. While a higher crosslinking density increases tensile strength, it reduces elongation at break and limits water transport due to reduced pore size, leading to lower overall shrinkage (Fig.S14).

3.3. Multimodal sensing performances of integrated hydrogel system

The conductivity of hydrogels with varying PANI contents is

illustrated in Fig. 3a. As the concentration of the conductive polymer increases, the conductivity of the $(\text{PVA})_2\text{PNIPAM}_{0.6}/\text{PANI}$ hydrogel increases accordingly. Fig. 3b shows a schematic diagram of the structural changes of the hydrogel during cyclic stretching and recovery. When the $(\text{PVA})_2\text{PNIPAM}_{0.6}/\text{PANI}_{0.2}/\text{P(VDF-TrFE)}$ actuator is stretched, the internal PANI network is destroyed, resulting in an increase in resistance. After release, the network partially recovers and the resistance decreases. This reversible piezoresistive behavior makes strain sensing possible. To intuitively demonstrate this effect, we integrated the hydrogel into a circuit as a wire to power an LED (Fig. 3c). During stretching, the LED dims due to the interruption of conduction; when relaxed, the brightness recovers, indicating that the conductive pathway has been restored. The hydrogel sensor exhibits a sensitivity of 0.936 with a highly linear response in the strain range 0%–110% (Fig. 3d), confirming its excellent sensitivity and stability. To assess its strain-dependent electrical properties, the hydrogel sensor was subjected to incremental tensile strains of 20%, 40%, 60%, 80%, and 100%, with corresponding holding and recovery phases (Fig. 3e). The relative resistance change ($\Delta R/R_0$) increases proportionally with strain, stabilizes during the holding phase, and returns to baseline upon release, indicating robust electrical stability under cyclic tensile deformation. The repeatability of the hydrogel sensor was evaluated through ten loading-unloading cycles at 20%, 40%, and 60% strains (Fig. 3f). The consistent signal output across cycles confirms its reliability. Additionally, the sensor's response time was analyzed, revealing a loading time of 235 ms and an unloading time of 292 ms during rapid stretching (Fig. S15), demonstrating its fast response capability.

The preparation process of the piezoelectric film is shown in Fig.S16. To assess its performance in motion sensing, the bending deformation of $(\text{PVA})_2\text{PNIPAM}_{0.6}/\text{PANI}_{0.2}/\text{P(VDF-TrFE)}$ integrated hydrogel actuator (fabrication process illustrated in Fig.S17) was induced via a mechanical testing system (Fig.S18). A controlled bend ranging from 0° to 90° was applied to the integrated hydrogel actuator (Fig. 3g). For angles below 60° , the sensor demonstrates a sensitivity of 0.414, while for angles between 60° and 90° , the sensitivity increases to 0.833. Since both ends of the actuator are fixed, bending causes progressive tensile strain on the outer surface, leading to further disruption of the PANI network and corresponding increases in resistance. This resistance-based sensing mechanism complements the piezoelectric response and provides accurate deformation feedback. The detection of discontinuous bending is depicted in Fig. 3h, where $\Delta R/R_0$ exhibits stepwise increases at 30° , 60° , and 90° . Upon returning the integrated hydrogel actuator to its original position, the resistance gradually decreases, indicating the reformation of the conductive network. Repeated bending tests at these angles further confirm the sensor's reproducibility and reliability (Fig. 3i). When the P(VDF-TrFE) piezoelectric film is bent, polarized charges will be generated at the upper and lower electrodes, resulting in a voltage output. During the recovery process, due to the bending in opposite directions, polarized charges of opposite polarities are generated at the upper and lower electrodes, thus resulting in an opposite voltage output. Fig.S19 presents the charge dissipation process during rapid and slow bending conditions. When the piezoelectric film is bent rapidly ($t < \Delta t$), it reaches the target deformation within the response time Δt , producing a maximum output voltage corresponding to the bending angle. Conversely, under slow bending ($t > \Delta t$), the piezoelectric layer requires more time to reach the target deformation. In this scenario, the rate of charge generation gradually equilibrates with the rate of charge loss, leading to partial charge dissipation through the material or external circuit prior to the completion of deformation. Consequently, the resulting output voltage remains consistent. Thus, the peak output voltage is primarily determined by the magnitude of deformation achieved within the response time Δt . Additionally, the piezoelectric sensor exhibits polarity-dependent voltage output under different bending directions (Fig.S20). The embedded pre-polarized P(VDF-TrFE) layer responds to mechanical bending by generating a piezoelectric voltage. As shown in Fig. 3j, bending in opposite directions produces voltage signals

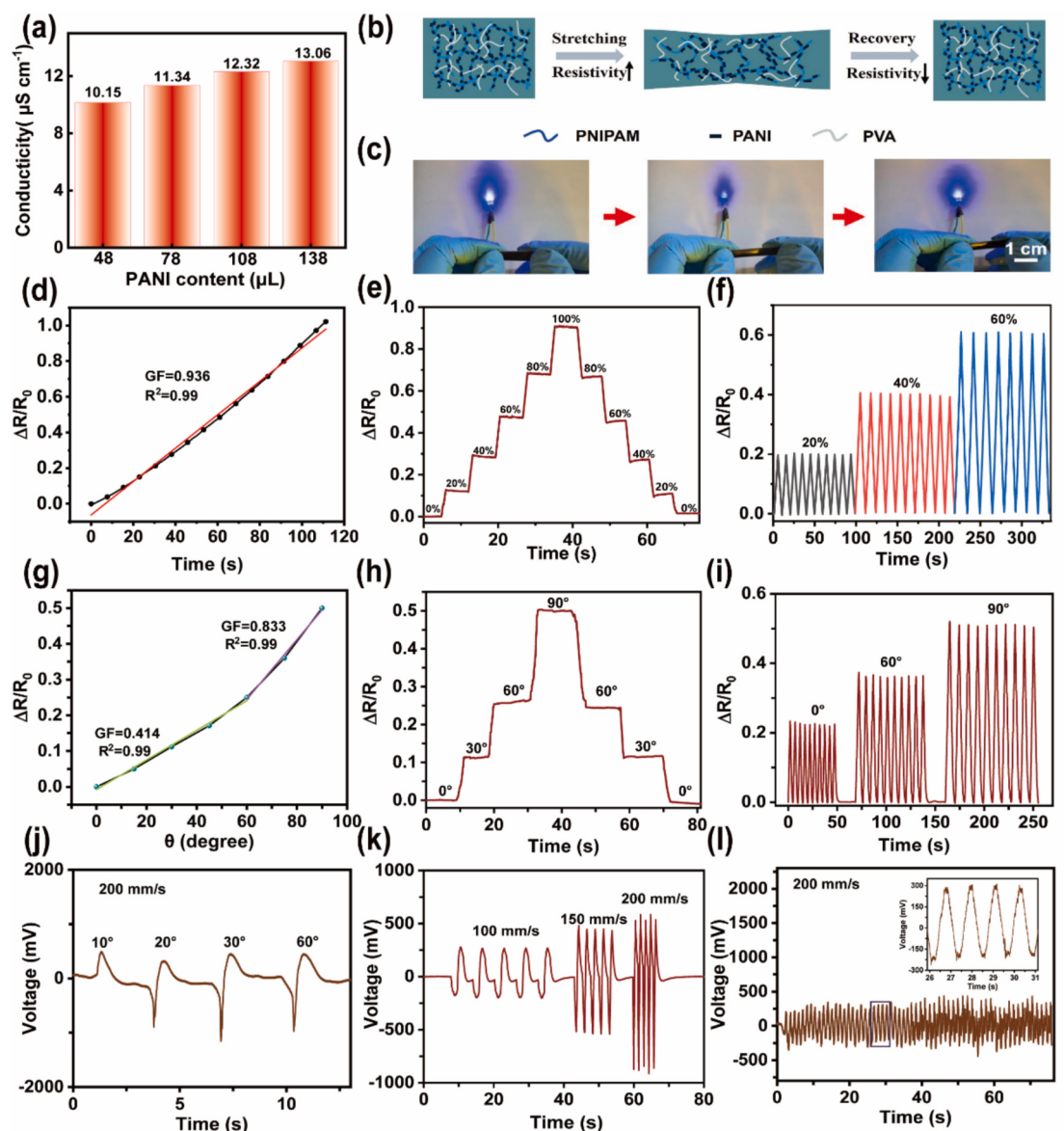


Fig. 3. (a) Conductivity of $(\text{PVA})_2\text{PNIPAM}_{0.6}/\text{PANI}_{0.2}$ integrated hydrogels as a function of varying PANI content. (b) Schematic illustration of resistivity changes during cyclic stretching and relaxation of the integrated hydrogel system. (c) Schematic representation of brightness fluctuations in an LED circuit utilizing the integrated hydrogel under stretching conditions. (d) Relationship between the relative resistance change ($\Delta R/R_0$) of the integrated hydrogel sensor and applied tensile strain. (e) Dynamic changes in relative resistance during stepwise loading and unloading cycles. (f) Long-term stability assessment of relative resistance over multiple cycles at different maximum tensile strains (20%, 40%, and 60%). (g) Quantitative relationship between the relative resistance change of the integrated hydrogel actuator and bending angle. (h) Relative resistance variations of the integrated hydrogel actuator at distinct bending angles. (i) Consistency evaluation of relative resistance changes in the integrated hydrogel actuator across multiple bending cycles at various bending angles. (j) Output voltage characteristics of the integrated hydrogel actuator at different bending angles. (k) Voltage output behavior of the integrated hydrogel actuator under varying bending speeds. (l) Repeatability analysis of integrated hydrogel actuator during cyclic bending tests.

of opposite polarity-leftward bending yields a positive voltage that returns to zero upon relaxation, followed by a negative spike during recovery. Reversing the bending direction inverts the polarity. While the final bending angle does not affect voltage amplitude under constant deformation speed, increasing the loading rate enhances voltage output due to faster charge accumulation (Fig. 3k). Long-term cyclic bending confirms good signal stability and durability (Fig. 3l). A schematic explanation of the piezoelectric sensing mechanism is provided in Fig. S21.

3.4. Photothermal actuation and self-sensing behavior of integrated sensing-actuation systems

Beyond its electrical responsiveness, the integrated $(\text{PVA})_2\text{PNIPAM}_{0.6}/\text{PANI}_{0.2}$ hydrogel also exhibits remarkable photothermal actuation capabilities, further expanding its potential for smart sensing and actuation applications. As illustrated in Fig. 4a, the integration of PANI into the hydrogel significantly enhances its photothermal conversion capability. Upon exposure to incident light, PANI efficiently absorbs and converts light energy into heat, leading to a localized temperature rise. Once the hydrogel reaches its critical transition temperature, a phase transition occurs, triggering water expulsion and resulting in macroscopic bending. This structural deformation is accompanied by a

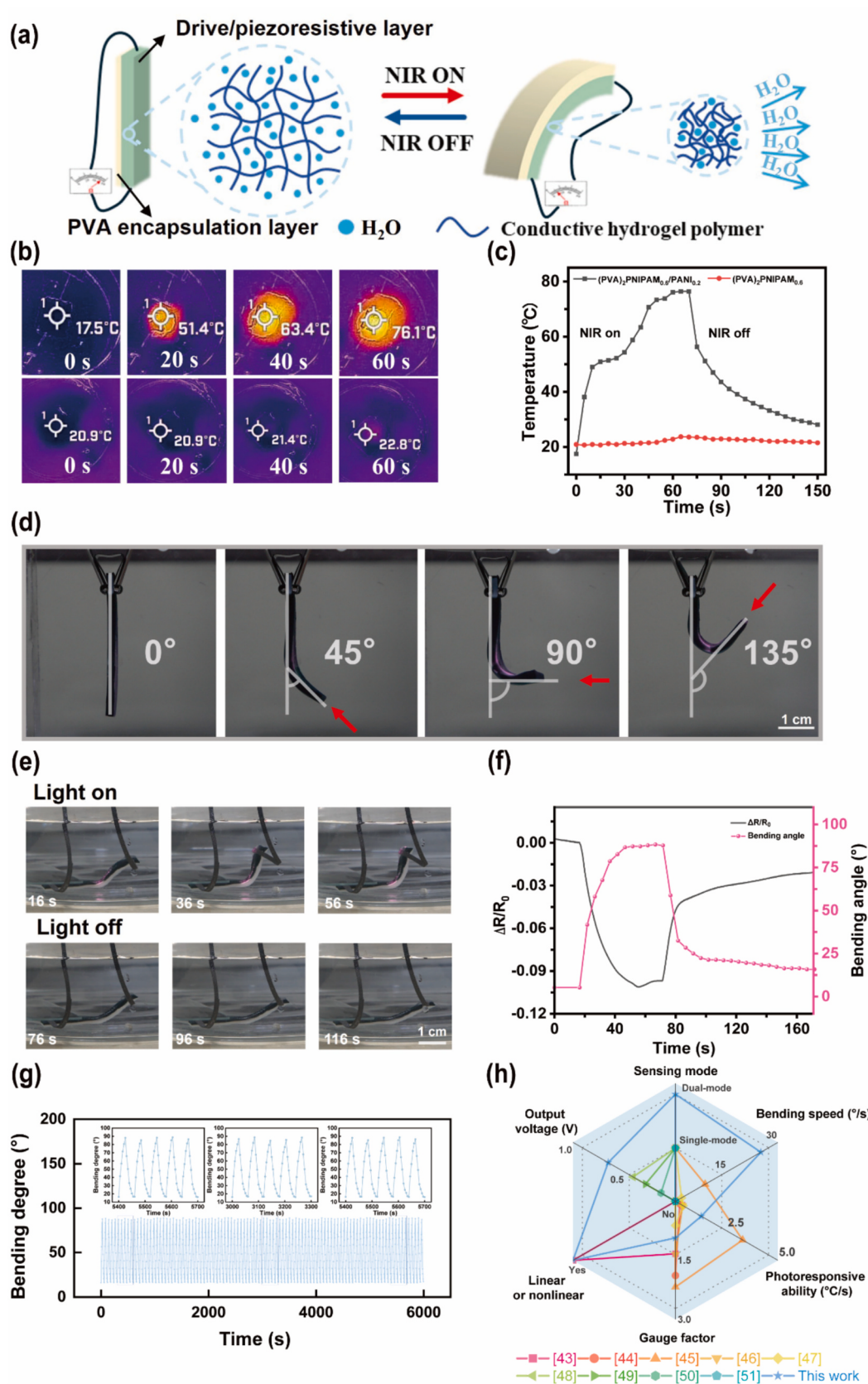


Fig. 4. (a) Schematic illustration of the integrated hydrogel's water loss, bending behavior, and corresponding resistance change. (b) Infrared thermal images. (c) Plot of temperature variation over time. (d) Bending configurations of the integrated hydrogel at various angles under NIR irradiation in an aqueous environment. (e) Bending response of integrated hydrogels in water under near-infrared irradiation. (f) Correlation between bending angle and real-time self-sensing resistance change. (g) The angle change of 100 drive-recovery cycles under near-infrared irradiation in water (h) Radar chart comparing the performance of this work with other hydrogel actuators and piezoelectric sensors [43–51].

corresponding decrease in relative resistance. Fig. 4b and c illustrate the dynamic temperature changes of the hydrogel under NIR light irradiation in an aqueous environment. The PANI-integrated hydrogel exhibits a rapid temperature increase, reaching 76.1 °C within 60 s, which

highlights its superior photothermal performance.

In contrast, a PANI-free hydrogel shows negligible temperature variation under the same conditions, confirming the crucial role of PANI in facilitating efficient light-to-heat energy conversion. To assess long-

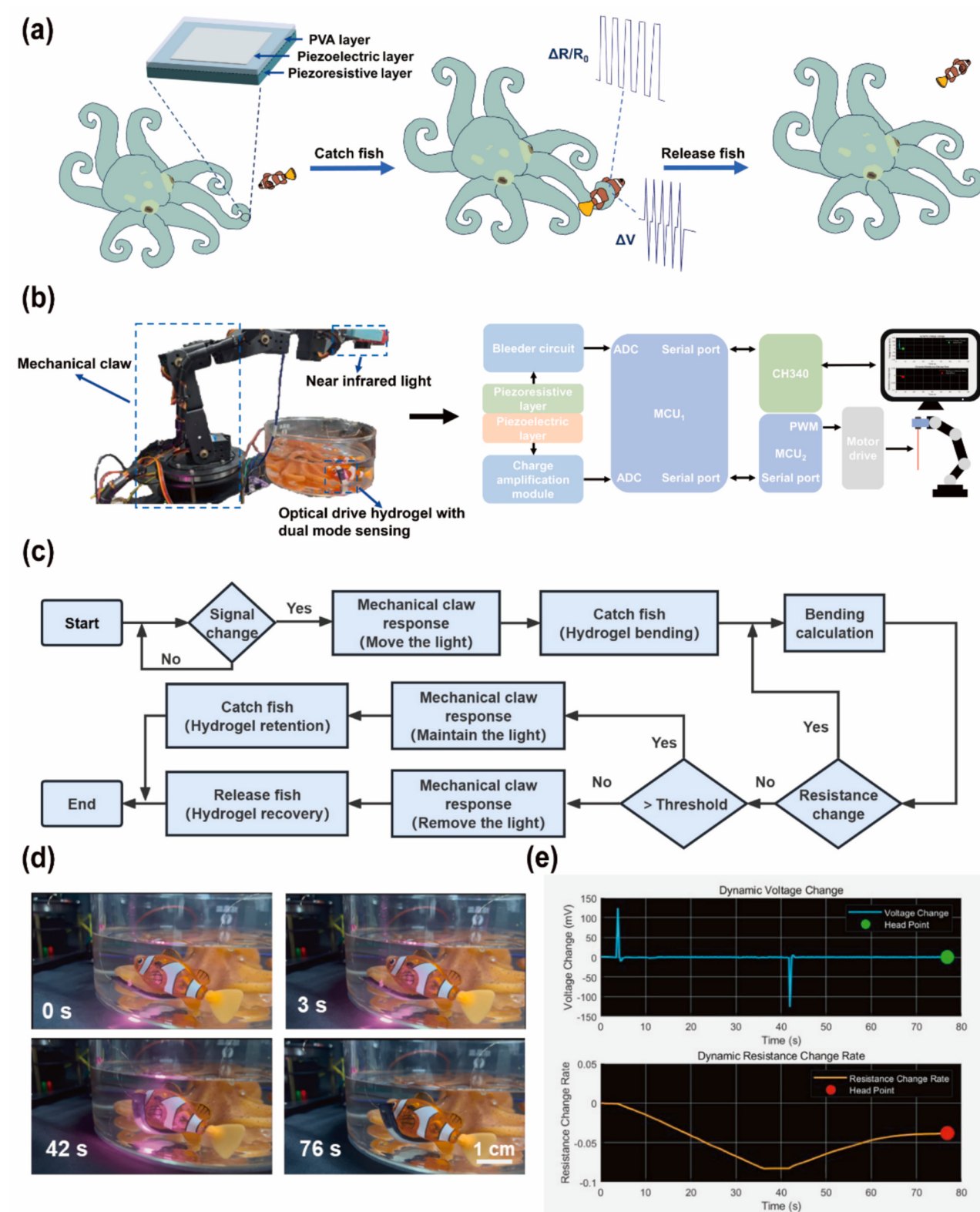


Fig. 5. (a) Schematic diagram of the octopus hunting and release process; (b) optical image and hardware mechanism diagram of the intelligent hunting system of bionic octopus tentacle; (c) flowchart of the program for the intelligent hunting system of bionic octopus tentacle; (d) optical image of the bionic octopus grasping process; (e) changes in electrical signals during the grasping process.

term photothermal durability, we conducted 100 cycles of NIR-induced heating and actuation (Fig. S22 and Fig. 4g). Throughout these cycles, both the peak temperature and actuation angle remained stable, indicating excellent photothermal and mechanical stability. Enlarged views of selected cycles confirm the consistency of the actuation response across different time points. The integrated hydrogel actuator displays robust and reversible NIR-driven actuation. As shown in Fig. S23 and Movie S1, it can lift a load in air, while Fig. S24 and Movie S2 demonstrate its rapid underwater actuation and recovery. This dynamic behavior supports its potential for soft robotic applications. Notably, the integrated hydrogel exhibits autonomous ray-tracing behavior, as demonstrated in Fig. 4d. Upon exposure to incident light, the integrated hydrogel dynamically adjusts its bending direction to align with the light source. This self-orienting response is governed by the interplay between photothermal actuation and heat dissipation through water cooling, resulting in stable light-targeting behavior. Furthermore, the integrated hydrogel exhibits simultaneous actuation and self-sensing capabilities. As shown in Fig. 4e and f, along with Movie S3, the integrated hydrogel undergoes underwater self-sensing processes. Upon NIR light exposure, it rapidly bends, and real-time resistance measurements reveal a symmetric change corresponding to its deformation. To ensure durability, SEM images taken before and after 100 cycles of photothermal actuation confirm the structural integrity of the porous network (Fig. S25), with no observable degradation. These results collectively demonstrate that the actuator maintains excellent actuation efficiency, sensing performance, and morphological stability under prolonged NIR cycling. To contextualize its sensing performance, we conducted a comparative analysis with representative hydrogel-based actuators and sensors reported in recent literature [43–51]. As summarized in the radar chart (Fig. 4h), the (PVA)₂PNIPAM_{0.6}/PANI_{0.2}/P(VDF-TrFE) actuator exhibits a balanced integration of key features: fast photothermal responsiveness, high bending speed, dual-mode sensing, good linearity of output signals, a moderate gauge factor, and relatively high piezoelectric voltage output. This combination positions our device as a competitive and multifunctional platform suitable for next-generation soft robotics, wearable electronics, and intelligent sensing applications.

3.5. Bionic flexible actuators with dual-mode self-sensing behavior

Inspired by the biological hunting behavior of octopus tentacles (Fig. 5a), this study innovatively constructed a bionic flexible robotic arm system with proprioceptive capabilities based on the dual-mode self-sensing actuator prepared in the previous stage. The system achieves synergistic integration of robotic actuation and state monitoring through heterogeneous integration of the hydrogel's dual actuation-sensing functionality with P(VDF-TrFE) piezoelectric films, leveraging complementary piezoresistive and piezoelectric effects. To evaluate signal stability, the actuator underwent 100 NIR-induced bending-recovery cycles, during which both piezoresistive and piezoelectric signals were recorded (Fig. S26). The results show excellent repeatability with minimal signal drift, confirming stable electrical performance during prolonged operation. The bio-inspired system employs a modular architecture comprising the STM32F103C8T6 microcontroller (STMicroelectronics) to construct a multi-channel signal acquisition system (Fig. S27). This system includes: (1) a precision voltage divider circuit for acquiring piezoresistive signals, and (2) a charge amplification module for conditioning piezoelectric signals (Fig. 5b). A CH340 USB-serial converter facilitates bidirectional communication between the acquisition system and the host computer. The detailed control algorithm flow is illustrated in Fig. 5c. Upon detecting a target within the operational range, the control system activates the NIR driver module to induce photothermal bending of the bio-inspired octopus gripper, thereby enabling grasping maneuvers (Fig. 5d). During this process, the dual-mode sensing system continuously monitors the dynamic response of the actuator in real time: the piezoresistive signal quantifies the degree of tentacle bending and estimates prey size, while the piezoelectric

signal captures strain rate and direction information. As depicted in Fig. 5e, when the rate of resistance change falls below the threshold and remains consistently low, the control system determines that the capture action is complete and subsequently deactivates the NIR source. This allows the hydrogel network to revert to its initial morphology via the dissolution effect, accurately mimicking the biological process of an octopus's hunt-release behavior (Supporting Material Movie S4). This bionic intelligent system introduces an innovative proprioceptive paradigm for soft-bodied robotics, showcasing enhanced operational capabilities through advanced self-sensing mechanisms and enabling applications in high-stakes environments such as deep-sea exploration and precision-driven medical procedures.

4. Conclusion

In this study, we developed an intelligent hydrogel system that integrates actuation and dual-mode sensing capabilities. By engineering a PNIPAM hydrogel with a co-solvent-induced open-pore microstructure, it achieved significant enhancements in mechanical performance, resulting in a 4.1-fold increase in maximum stress tolerance and a 1.9-fold improvement in Young's modulus compared to conventional hydrogels. The optimized structure exhibited rapid thermal responsiveness, shrinking to 39% of its original volume within 35 s at 60 °C. Utilizing a low-temperature one-pot synthesis method enabled uniform integration of a PANI conductive network, thereby endowing the composite with photothermal conversion efficiency (reaching 76.1 °C under NIR irradiation within 60 s) and strain-sensing functionality. Further integration of a P(VDF-TrFE) piezoelectric film facilitated dual-mode sensing, allowing for simultaneous monitoring of dynamic pressure and static deformation. This bionic design strategy was further validated through a closed-loop control system that demonstrated muscle-like adaptability. The synergistic fusion of actuation and bimodal sensing establishes a new paradigm for intelligent soft robotics, offering enhanced possibilities for natural human-robot interaction.

Supplementary data to this article can be found online at <https://doi.org/10.1016/j.cej.2025.165091>.

CRediT authorship contribution statement

Chengnan Qian: Writing – original draft, Software, Methodology, Data curation. **Ping Guo:** Software, Methodology, Data curation, Conceptualization. **Ruofei Wang:** Validation, Software. **Xuanzi Luo:** Software, Data curation. **Yang Yu:** Validation, Software. **Lin Cheng:** Writing – original draft, Supervision, Project administration. **Aiping Liu:** Writing – review & editing, Supervision, Project administration, Funding acquisition.

Declaration of competing interest

The authors declare that they have no known competing financial interests or personal relationships that could have appeared to influence the work reported in this paper.

Acknowledgements

This work was supported by the National Natural Science Foundation of China (Nos. 12272351, 62401509 and 12372168), the Zhejiang Provincial Natural Science Foundation of China (Nos. LZ24A020004 and LRG25A020001), and the Youth Top-notch Talent Project of Zhejiang Ten Thousand Plan of China (No. ZJWR0308010).

Data availability

Data will be made available on request.

References

- [1] Z.L. Hou, X.B. Li, X.R. Zhang, W.D. Zhang, Z.L. Wang, H.L. Zhang, A bioinspired, self-powered, flytrap-based sensor and actuator enabled by voltage triggered hydrogel electrodes, *Nano Res.* 16 (2023) 10198–10205, <https://doi.org/10.1007/s12274-023-5621-2>.
- [2] M.S. Kim, J.K. Heo, H. Rodrigue, H.T. Lee, S. Pané, M.W. Han, S.H. Ahn, Shape memory alloy (SMA) actuators: the role of material, form, and scaling effects, *Adv. Mater.* 35 (2023), <https://doi.org/10.1002/adma.202208517>, 2208517.
- [3] A.S. Kuenstler, H. Kim, R.C. Hayward, Liquid crystal elastomer waveguide actuators, *Adv. Mater.* 31 (2019) 1901216, <https://doi.org/10.1002/adma.201901216>.
- [4] X.M. Zhang, P. Xue, X. Yang, C. Valenzuela, Y.H. Chen, P.F. Lv, Z.K. Wang, L. Wang, X.H. Xu, Near-infrared light-driven shape-programmable hydrogel actuators loaded with metal-organic frameworks, *ACS Appl. Mater. Inter.* 14 (2022) 11834–11841, <https://doi.org/10.1021/acsmami.1c24702>.
- [5] J. He, Z.Q. Chen, Y.H. Xiao, X.N. Cao, J. Mao, J.J. Zhao, X. Gao, T.F. Li, Y.W. Luo, Intrinsically anisotropic dielectric elastomer fiber actuators, *Mater. Lett.* 4 (2022) 472–479, <https://doi.org/10.1021/acsmaterialslett.1c00742>.
- [6] Ping Guo, Zhaoxin Zhang, Chengnan Qian, Ruofei Wang, Lin Cheng, Ye Tian, Wu Huaping, Shuze Zhu, Aiping Liu, Programming hydrogen bonds for reversible elastic-plastic phase transition in a conductive stretchable hydrogel actuator with rapid ultra-high-density energy conversion and multiple sensory properties, *Adv. Mater.* 36 (2024) 2410324, <https://doi.org/10.1002/adma.202410324>.
- [7] Q. Pang, H.T. Hu, H.Q. Zhang, B.B. Qiao, L. Ma, Temperature-responsive ionic conductive hydrogel for strain and temperature sensor, *ACS Appl. Mater. Inter.* 14 (2022) 26536–26547, <https://doi.org/10.1021/acsmami.2c06952>.
- [8] X.S. Wei, Q.J. Wu, L. Chen, Y. Sun, L. Chen, C.M. Zhang, S.S. Li, C.X. Ma, S. H. Jiang, Remotely controlled light/electric/magnetic multiresponsive hydrogel for fast actuators, *ACS Appl. Mater. Inter.* 15 (2023) 10030–10043, <https://doi.org/10.1021/acsmami.2c22831>.
- [9] A. López-Díaz, A. Martín-Pacheco, A.M. Rodríguez, M.A. Herrero, A.S. Vázquez, E. Vázquez, Concentration gradient-based soft robotics: hydrogels out of water, *Adv. Funct. Mater.* 30 (2020) 2004417, <https://doi.org/10.1002/adfm.2020004417>.
- [10] Y. Cao, Y. Cheng, G. Za, Near-infrared light, magneto, and pH-responsive GO-Fe₃O₄/Poly(N-isopropylacrylamide)/alginate nanocomposite hydrogel microcapsules for controlled drug release, *Langmuir* 37 (2021) 5522–5530, <https://doi.org/10.1021/acs.langmuir.1c00207>.
- [11] H. Chen, X.Y. Zhang, L. Shang, Z.Q. Su, Programmable anisotropic hydrogels with localized photothermal/magnetic responsive properties, *Adv. Sci.* 9 (2022) 2202173, <https://doi.org/10.1002/advs.202202173>.
- [12] Q.L. Zhu, W.X. Liu, O. Khoruzhenko, J. Breu, H.Y. Bai, W. Hong, Q. Zheng, Z.L. Wu, Closed twisted hydrogel ribbons with self-sustained motions under static light irradiation, *Adv. Mater.* 36 (2024) 2314152, <https://doi.org/10.1002/adma.2023214152>.
- [13] N. Chen, Y. Zhou, Y.P. Chen, Y.Y. Mi, S.S. Zhao, W. Yang, S. Che, H.C. Liu, F. J. Chen, C. Xu, G. Ma, X. Peng, Y.F. Li, Conductive photo-thermal responsive bifunctional hydrogel system with self-actuating and self-monitoring abilities, *Nano Res.* 15 (2022) 7703–7712, <https://doi.org/10.1007/s12274-022-4394-3>.
- [14] Y.C. Zhang, J.X. Liao, T. Wang, W.X. Sun, Z. Tong, Polyampholyte hydrogels with pH modulated shape memory and spontaneous actuation, *Adv. Funct. Mater.* 28 (2018) 1707245, <https://doi.org/10.1002/adfm.201707245>.
- [15] G. Davidson-Rosenfeld, X.H. Chen, Y.L. Qin, Y. Ouyang, Y.S. Sohn, Z.Z. Li, R. Nechushtai, I. Willner, Stiffness-switchable, biocatalytic pH-responsive DNA-functionalized polyacrylamide cryogels and their mechanical applications, *Adv. Funct. Mater.* 34 (2024) 2306586, <https://doi.org/10.1002/adfm.202306586>.
- [16] H. Liu, H.X. Chu, H.L. Yuan, D.L. Li, W.S. Deng, Z.W. Fu, R.N. Liu, Y.Y. Liu, Y. X. Han, Y.P. Wang, Y. Zhao, X.Y. Cui, Y. Tian, Bioinspired multifunctional self-sensing actuated gradient hydrogel for soft-hard robot remote interaction, *Nanomicro. Lett.* 16 (2024) 69, <https://doi.org/10.1007/s40820-023-01287-z>.
- [17] M.K. Shin, G.M. Spinks, S.R. Shin, S.I. Kim, S.J. Kim, Nanocomposite hydrogel with high toughness for bioactuators, *Adv. Mater.* 21 (2009) 1712, <https://doi.org/10.1002/adma.200802205>.
- [18] C.S. Park, Y.W. Kang, H. Na, J.Y. Sun, Hydrogels for bioinspired soft robots, *Prog. Polym. Sci.* 150 (2024) 101791, <https://doi.org/10.1016/j.progpolymsci.2024.101791>.
- [19] F. Hao, L.Y. Wang, B.L. Chen, L. Qiu, J. Nie, G.P. Ma, Bifunctional smart hydrogel dressing with strain sensitivity and NIR-responsive performance, *ACS Appl. Mater. Inter.* 13 (2021) 46938–46950, <https://doi.org/10.1021/acsmami.1c15312>.
- [20] A. Halperin, M. Kriger, F.M. Winnik, Poly(N-isopropylacrylamide) phase diagrams: fifty years of research, *Angew. Chem. Int. Ed.* 54 (2015) 15342–15367, <https://doi.org/10.1002/anie.201506663>.
- [21] C. Liu, J.N. Luo, H.D. Liu, J.X. Fu, H.F. Liu, H. Tang, Z.K. Deng, J.Z. Wu, Y.F. Li, C. T. Liu, S.Q. Peng, J.X. Hu, T.T. Ren, J.H. Zhou, Y.C. Qiao, Intelligent soft quasi-organism equipped with sensor-driven integrated tentacles, *Adv. Funct. Mater.* 34 (2024) 2404333, <https://doi.org/10.1002/adfm.202404333>.
- [22] Y. Zhang, X.M. Zhou, N. Zhang, J.Q. Zhu, N.N. Bai, X.Y. Hou, T. Sun, G. Li, L. Y. Zhao, Y.C. Chen, L. Wang, C.F. Guo, Ultrafast piezocapacitive soft pressure sensors with over 10 kHz bandwidth via bonded microstructured interfaces, *Nat. Commun.* 15 (2024) 3048, <https://doi.org/10.1038/s41467-024-47408-z>.
- [23] J.T. Qu, Q.J. Yuan, Z.K. Li, Z.Q. Wang, F. Xu, Q.G. Fan, M. Zhang, X. Qian, X. Q. Wang, X.H. Wang, M.Y. Xu, All-in-one strain-triboelectric sensors based on environment-friendly ionic hydrogel for wearable sensing and underwater soft robotic grasping, *Nano Energy* 111 (2023) 108387, <https://doi.org/10.1016/j.nanoen.2023.108387>.
- [24] W.Y. Wang, P.S. Guo, X. Liu, M.J. Chen, J.H. Li, Z.G. Hu, G.D. Li, Q. Chang, K. M. Shi, X.L. Wang, K. Lei, Fully polymeric conductive hydrogels with low hysteresis and high toughness as multi-responsive and self-powered wearable sensors, *Adv. Funct. Mater.* 34 (2024) 2316346, <https://doi.org/10.1002/adfm.202316346>.
- [25] X.Y. Ding, Y.R. Yu, W.Z. Li, F.K. Bian, H.C. Gu, Y.J. Zhao, Multifunctional carbon nanotube hydrogels with on-demand removability for wearable electronics, *Nano Today* 54 (2024) 102124, <https://doi.org/10.1016/j.nantod.2023.102124>.
- [26] H.J. Li, Y. Liang, G.R. Gao, S.X. Wei, Y.K. Jian, X.X. Le, W. Lu, Q.O. Liu, J. W. Zhang, T. Chen, Asymmetric bilayer CNTs-elastomer/hydrogel composite as soft actuators with sensing performance, *Chem. Eng. J.* 415 (2021) 128988, <https://doi.org/10.1016/j.cej.2021.128988>.
- [27] P. Kościelniak, A. Więckowska, M. Karbarz, K. Kaniewska, Nanocomposite hydrogel for skin motion sensing—an antifreezing, nanoreinforced hydrogel with decorated AuNP as a multicrosslinker, *J. Colloid Interface Sci.* 674 (2024) 392–404, <https://doi.org/10.1016/j.jcis.2024.06.186>.
- [28] G.M. Wei, J.J. Wei, J. Zhou, Y.G. Chen, D.B. Wu, Q.G. Wang, MoS₂ nanosheet initiated smart polymeric hydrogel for NIR-driven Ag(I) enrichment, *Chem. Eng. J.* 382 (2020) 123018, <https://doi.org/10.1016/j.cej.2019.123018>.
- [29] Z.C. Sun, C. Wei, W.T. Liu, H. Liu, J.H. Liu, R. Hao, M.M. Huang, S.Q. He, Two-dimensional MoO₂ nanosheet composite hydrogels with high transmittance and excellent photothermal property for near infrared responsive actuators and microvalves, *ACS Appl. Mater. Inter.* 13 (2021) 33404–33416, <https://doi.org/10.1021/acsmami.1c04110>.
- [30] Q. Yan, R.J. Ding, H.W. Zheng, P.Y. Li, Z.L. Liu, Z. Chen, J.H. Xiong, F.H. Xue, X. Zhao, Q.Y. Peng, X.D. He, Bio-inspired stimuli-responsive Ti₃C₂T_x/PNIPAM anisotropic hydrogels for high-performance actuators, *Adv. Funct. Mater.* 33 (2023) 2301982, <https://doi.org/10.1002/adfm.202301982>.
- [31] S.S. Ma, P. Xue, C. Valenzuela, X. Zhang, Y.H. Chen, Y. Liu, L. Yang, X.H. Xu, L. Wang, Highly stretchable and conductive MXene-encapsulated liquid metal hydrogels for bioinspired self-sensing soft actuators, *Adv. Funct. Mater.* 34 (2024) 2309899, <https://doi.org/10.1002/adfm.202309899>.
- [32] Z.W. Wang, H.W. Zhou, W.X. Chen, Q.Z. Li, B. Yan, X.L. Jin, A.J. Ma, H.B. Liu, W. F. Zhao, Dually synergistic network hydrogels with integrated mechanical stretchability, thermal responsiveness, and electrical conductivity for strain sensors and temperature alertors, *ACS Appl. Mater. Inter.* 10 (2018) 14045–14054, <https://doi.org/10.1021/acsmami.8b02060>.
- [33] Y.S. Zhao, C.Y. Lo, L.C. Ruan, C.H. Pi, C. Kim, Y. Alsaid, I. Frenkel, R. Rico, T. C. Tsao, X.M. He, Somatosensory actuator based on stretchable conductive photothermally responsive hydrogel, *Sci. Robot.* 6 (2021) 5483, <https://doi.org/10.1126/scirobotics.abd5483>.
- [34] C.Z. Lv, Z.J. Zhou, Y.Q. Li, S.R. Lu, Y.K. Bai, Multi-responsive shape memory porous composites for self-powered sensors and self-sensing actuators, *Chem. Eng. J.* 477 (2023) 147059, <https://doi.org/10.1016/j.cej.2023.147059>.
- [35] K. Wang, X. Zhang, C. Li, X.Z. Sun, Q.H. Meng, Y.W. Ma, Z.X. Wei, Chemically crosslinked hydrogel film leads to integrated flexible supercapacitors with superior performance, *Adv. Mater.* 27 (2015) 7451–7457, <https://doi.org/10.1002/adma.201503543>.
- [36] Y.L. Zou, C. Chen, Y.J. Sun, S.C. Gan, L.B. Dong, J.H. Zhao, J.H. Rong, Flexible, all-hydrogel supercapacitor with self-healing ability, *Chem. Eng. J.* 418 (2021) 128616, <https://doi.org/10.1016/j.cej.2021.128616>.
- [37] D. Mukherji, C.M. Marques, K. Kremer, Polymer collapse in miscible good solvents is a generic phenomenon driven by preferential adsorption, *Nat. Commun.* 5 (2014) 4882, <https://doi.org/10.1038/ncomms5882>.
- [38] Y. Alsaid, S. Wu, D. Wu, Y. Du, L. Shi, R. Khodambashi, R. Rico, M. Hua, Y. Yan, Y. Zhao, D. Atukes, X. He, Tunable sponge-like hierarchically porous hydrogels with simultaneously enhanced diffusivity and mechanical properties, *Adv. Mater.* 33 (2021) 2008235, <https://doi.org/10.1002/adma.202008235>.
- [39] C.H. Qian, Q.Y. Li, C. Chen, L. Han, Q.S. Han, L.K. Liu, Z.C. Lu, A stretchable and conductive design based on multi-responsive hydrogel for self-sensing actuators, *Chem. Eng. J.* 454 (2023) 140263, <https://doi.org/10.1016/j.cej.2023.140263>.
- [40] J.J. Zhang, L.T. Zheng, Z.J. Wu, L. Wang, Y.J. Li, Thermoresponsive bilayer hydrogel with switchable bending directions as soft actuator, *Polymer* 253 (2022) 124998, <https://doi.org/10.1016/j.polymer.2022.124998>.
- [41] Y.Q. Li, Q. Gong, X.H. Liu, Z.B. Xia, Y. Yang, C. Chen, C.H. Qian, Wide temperature-tolerant polyaniline/cellulose/polyacrylamide hydrogels for high-performance supercapacitors and motion sensors, *Carbohydr. Polym.* 267 (2021) 118207, <https://doi.org/10.1016/j.carbpol.2021.118207>.
- [42] M.A. Darabi, A. Khosrozadeh, Y. Wang, N. Ashammakhi, H. Alem, A. Erdem, Q. Chang, K.G. Xu, Y.Q. Liu, G.X. Luo, A. Khademhosseini, M. Xing, An alkaline based method for generating crystalline, strong, and shape memory polyvinyl alcohol biomaterials, *Adv. Sci.* 7 (2020) 1902740, <https://doi.org/10.1002/advs.201902740>.
- [43] H.J. Li, Y. Liang, G.R. Gao, S.X. Wei, Y.K. Jian, X.X. Le, W. Lu, Q.O. Liu, J. W. Zhang, T. Chen, Asymmetric bilayer CNTs-elastomer/hydrogel composite as soft actuators with sensing performance, *Chem. Eng. J.* 415 (2021) 128988, <https://doi.org/10.1016/j.cej.2021.128988>.
- [44] T.Z. Jiang, S.L. Gai, Y.Q. Yin, Z.W. Sun, B.C. Zhou, Y.B. Zhao, H. Ding, Anees Ahmad Ansari, Piaoping Yang, A light/thermal cascaded-driven equipment for machine recognition inspired by water lilies using as multifunctional soft actuator, *Chem. Eng. J.* 495 (2024) 153348, <https://doi.org/10.1016/j.cej.2024.153348>.
- [45] M.T. Shang, S.S. Ma, J.F. Ma, L.Y. Guo, C. Liu, X.H. Xu, Somatosensory actuators based on light-responsive anisotropic hydrogel for storage encryption of information systems, *Chem. Eng. J.* 496 (2024) 153895, <https://doi.org/10.1016/j.cej.2024.153895>.
- [46] L.K. Liu, Y.Q. Li, Z.C. Lu, R.T. Miao, N. Zhang, Thermal and light-driven soft actuators based on a conductive polypyrrole nanofibers integrated poly(N-

- isopropylacrylamide) hydrogel with intelligent response, *J. Colloid Interface Sci.* 675 (2024) 336–346, <https://doi.org/10.1016/j.jcis.2024.07.017>.
- [47] Z.C. Sun, C.Y. Song, J.J. Zhou, C.B. Hao, W.T. Liu, H. Liu, J.F. Wang, M.M. Huang, S.Q. He, M.C. Yang, Rapid photothermal responsive conductive MXene nanocomposite hydrogels for soft manipulators and sensitive strain sensors, *Macromol. Rapid Commun.* 42 (2021) 2100499, <https://doi.org/10.1002/marc.202100499>.
- [48] J.L. Shi, F. Peng, T.T. Shan, J. Guo, C.J. Gao, G.Q. Zheng, Efficiently fabricated core-sheath piezoelectric sensor based on PVDF Microfibrillar bundle, *Macromol. Rapid Commun.* 46 (2025) 2400616, <https://doi.org/10.1002/marc.202400616>.
- [49] S. Taleb, M. Badillo, F.J. Flores-Ruiz, M. Acuautla, From synthesis to application: high-quality flexible piezoelectric sensors fabricated from tetragonal BaTiO₃/P(VDF-TrFE) composites, *Sensor Actuat A-Phys.* 361 (2023) 114585, <https://doi.org/10.1016/j.sna.2023.114585>.
- [50] Z.J. Zhou, C.Y. You, Y. Chen, W.M. Xia, N. Tian, Y. Li, C.K. Wang, Piezoelectric sensing performance of flexible P(VDF-TrFE)/PBDMS porous polymer materials, *Org. Electron.* 105 (2022) 106491, <https://doi.org/10.1016/j.orgel.2022.106491>.
- [51] L. Li, J.L. Pan, L.F. Chang, Z.H. Liu, G. Wu, Y. Hu, A MXene heterostructure-based piezionic sensor for wearable sensing applications, *Chem. Eng. J.* 482 (2024) 148988, <https://doi.org/10.1016/j.cej.2024.148988>.